



Size effect on melting temperatures of alumina nanocrystals: Molecular dynamics simulations and thermodynamic modeling



Nikhil Joshi¹, Nilkumar Mathur, Tejas Mane, Dilip Sundaram*

Indian Institute of Technology Gandhinagar, Palaj, Gujarat 382355, India

ARTICLE INFO

Article history:

Received 26 May 2017

Received in revised form 28 December 2017

Accepted 30 December 2017

Available online 8 January 2018

Keywords:

Melting point

Alumina

Nanocrystals

Size effect

MD simulations

Thermodynamic models

ABSTRACT

Molecular dynamics (MD) simulations and thermodynamic analysis are conducted to investigate size effect on melting point of alumina nanocrystals. Different geometries including spherical and cubic particles, planar thin films, and spherical shells are considered. The atomic interactions in MD simulations are captured using Vashishta et al.'s potential function. Thermophysical properties of concern such as the bulk melting point, latent heat, density, and surface free energy are calculated using MD simulations and fed as inputs to the thermodynamic models. Predictions of MD simulations are compared with those of thermodynamic melting models. For all cases, heterogeneous melting is observed, where nucleation of the melt phase occurred at the free surface and the melting front propagated into the interior regions of the crystal. Results suggest that the melting point drops sharply below a threshold particle size, which is a function of the geometry. The threshold particle size of spherical particles is greater than that of planar films. Melting point predictions are quite sensitive to the choice of thermodynamic model and thermophysical property values. To ascertain the effects of curvature and core size on shell melting point, melting points of planar semi-infinite films and spherical shells are calculated and compared. For particle sizes of concern to practical applications (~100 nm or greater), shell melting point is nearly independent of core size and the semi-infinite planar film approximation is reasonable to estimate the melting point of alumina shells. In this size regime, melting points of 2–4 nm thick spherical oxide shells vary roughly in the range of 1800–2350 K, which is relatively close to the bulk melting point. Results of the present study do not indicate an enormous depression in the melting point, as the previous works suggest. This implies that the melting point depression of the oxide layer cannot fully describe the scatter in the measured ignition temperature of aluminum particles.

© 2017 Elsevier B.V. All rights reserved.

1. Introduction

Owing to applications in propulsion and energy-conversion devices, aluminum particles have attracted a lot of attention [1]. Aluminum is widely used due to its high energy density, low cost, and relative safety [1]. Aluminum particles are usually covered by an aluminum oxide layer (Al_2O_3) of thickness ranging from 0.5 nm [2] to 4 nm [3]. The impervious nature of the oxide layer protects the aluminum core from unwanted oxidation, but delays the ignition process. As per the experimental observations of Friedman et al. [4], ignition of aluminum particles (15–65 μm) occurs at temperatures near the melting point of the oxide layer (~2350 K). Once the oxide layer melts, it contracts and forms a cap due to surface tension, thereby exposing the aluminum core to the ambi-

ent gas [1]. Furthermore, the species diffusion process speeds up, thereby accelerating reaction rate and resulting in ignition. Subsequent experimental studies, however, suggest that the measured ignition temperatures are as low as 1000 K [1]. Ignition temperature of aluminum particles depends on many parameters such as particle size, oxide layer thickness, type and concentration of oxidiser and heating rate. There is considerable uncertainty in the ignition temperature of aluminum particles.

Numerous theories have been advanced to explain the ignition mechanism of aluminum particles. Rozenband and Vaganova [5] suggested that cracks develop in the oxide layer due to mechanical stresses induced by the expansion of the aluminum core upon melting. The experimental observations of Rai et al. [6] also support this theory. Trunov et al. [7] suggests that polymorphic phase transformations in the oxide layer cause a significant increase in the oxide layer density, thereby producing openings in the oxide layer. The formation of cracks and openings in the oxide layer facilitates chemical reactions between the particle and oxidizing gas. Note that chemical reactions also result in healing of the oxide

* Corresponding author.

E-mail address: dilip.sundaram@iitgn.ac.in (D. Sundaram).

¹ Presently at Space Applications Centre, Indian Space Research Organization (ISRO), Ahmedabad, Gujarat, India.

layer, which tends to arrest these reactions. However, if the energy release increases the particle temperature to the melting temperature of the oxide layer, reactions can proceed in a self-sustained manner and ignition could be achieved. It is apparent the knowledge of melting point of the oxide layer is crucial in predicting ignition temperatures of aluminum particles. It is well known that melting temperatures of nanocrystals are size-dependent and deviates substantially from their bulk values [8]. As the oxide layer thickness is in the range of 0.5–4 nm and the particle size of concern is as low as few tens of nm, the melting point of oxide layer could be substantially lower than bulk melting point (~2300 K [9]–2350 K [1]). These could also possibly explain the wide scatter in the measured ignition temperatures of aluminum particles. As a result, it is important to investigate the size dependence of the melting point of the oxide layers.

Studies on melting of nano-scale aluminum oxide layers are quite scarce. Puri and Yang [10] studied melting of aluminum oxide layers of thickness in the range of 1–2.5 nm by means of molecular dynamics (MD) simulations using the Streitz–Mintmire potential. The melting point of the oxide layer was found to increase from 1130 K at 1.0 nm to 1313 K at 2.5 nm thickness. Note that these are substantially lower than the bulk value of ~2350 K. Note that the Streitz–Mintmire potential function was not shown to predict the melting temperatures of bulk alumina accurately. In a more recent work of Dreizin et al. [11], depression of the melting point of planar alumina films is quantified using equilibrium melting models. Melting points as low as ~1000 K was predicted. It is not immediately apparent that these results are applicable for oxide layers covering spherical aluminum particles. The melting point of the oxide shell is expected to be a function of core size and shell thickness. Furthermore, the validity of the melting model and its applicability to wide range of materials and conditions needs to be established.

High fidelity techniques such as molecular dynamics (MD) simulations can be used to get accurate predictions of melting points for a wide range of materials and conditions. MD simulations can predict the melting temperatures accurately under high heating rates, which are representative of conditions in many practical applications and laboratory experiments involving heating by laser irradiation and shock waves. The purpose of present work is to explore the size effect on melting temperatures of alumina nanocrystals. Different geometries are considered. Spherical oxide particles are of interest, as they are the primary combustion products of aluminum particles. Planar oxide films are considered as well as they are present in flake aluminum particles. Note that flake particles are of interest to propulsion applications due to their greater energy content and better safety and processing characteristics. Spherical oxide shells are considered due to their relevance to ignition of spherical aluminum particles. Furthermore, effects of core size and shell thickness on the melting point are explored. In addition to MD simulations, thermodynamic analysis of melting is conducted to investigate the melting point depression phenomenon. To facilitate comparison with MD predictions, thermo-physical properties obtained from MD simulations are fed as inputs to thermodynamic melting models. Implications of the results of the present study on ignition mechanism of aluminum particles are discussed.

2. Theoretical and computational framework

2.1. Molecular dynamics simulations

Molecular dynamics simulations are conducted for four different geometries: (1) spherical particles; (2) cubic particles; (3) semi-infinite planar films; and (4) spherical shells. Fig. 1 shows

the initial configurations for four different geometries considered in this study. A region is first created, with the shape and size based on the geometry and size of the nanocrystal under consideration. Atoms are generated using a set of fractional coordinates and lattice vectors. Spherical and cubic particles are placed at the centre of the simulation domain; the particles are surrounded by vacuum to ensure constancy of pressure throughout the simulation. Semi-infinite films are modeled by imposing periodic boundary conditions in two directions and by placing vacuum above and below the crystal in the third direction. Spherical shells are created by first removing a spherical region of atoms from a spherical particle and placing it in a vacuum.

The interatomic interactions are captured using the many-body potential function developed by Vashishta et al. [12]. The potential energy of the system can be written as

$$\begin{aligned} E &= \sum_{i < j} E_{ij}^{(2)}(r_{ij}) + \sum_{i < j < k} E_{jik}^{(3)}(r_{ij}, r_{ik}), \\ E_{ij}^{(2)}(r_{ij}) &= \frac{H_{ij}}{r_{ij}^{\eta_{ij}}} + \frac{Z_i Z_j}{r_{ij}} e^{-r_{ij}/\lambda} - \frac{D_{ij}}{2r_{ij}^4} e^{-r_{ij}/\xi} - \frac{W_{ij}}{r_{ij}^6}, \\ E_{jik}^{(3)}(r_{ij}, r_{ik}) &= R^{(3)}(r_{ij}, r_{ik}) P^{(3)}(\theta_{jik}), \\ R^{(3)}(r_{ij}, r_{ik}) &= B_{jik} \exp \left(\frac{\gamma}{r_{ij} - r_0} + \frac{\gamma}{r_{ik} - r_0} \right) \Theta(r_0 - r_{ij}) \Theta(r_0 - r_{ik}), \\ P^{(3)}(\theta_{jik}) &= \frac{(\cos \theta_{jik} - \cos \bar{\theta}_{jik})^2}{1 + C_{jik} (\cos \theta_{jik} - \cos \bar{\theta}_{jik})^2}, \end{aligned} \quad (1)$$

where r_{ij} is the interatomic distance, H_{ij} the strength of the steric repulsion, Z_i the effective charge in units of the electronic charge, D_{ij} and W_{ij} the strengths of the charge-dipole and van der Waals attractions, respectively, η_{ij} the exponents in the steric repulsion term, λ and ξ the screening lengths for Coulomb and charge dipole interactions, respectively, B_{jik} the strength of three-body interactions, θ_{jik} the angle formed by r_{ij} and r_{ik} , $\bar{\theta}_{jik}$ and C_{jik} the model constants, and $\Theta(r_0 - r_{ij})$ the step function. Table 1 lists the values of different parameters. The cut-off radius (r_c) for truncation of the potential is taken to be 6 Å.

Canonical (NVT) ensemble using the Nosé–Hoover thermostat is employed to investigate melting of spherical and cubic particles and spherical shells. Isothermal-isobaric (NPT) ensemble is used to study melting of semi-infinite planar films. Constancy of temperature and pressure is achieved using Nosé–Hoover thermostat and barostat. Barostat is applied only in the two directions in which periodic boundary conditions are imposed. The time step is chosen as 1 fs in order to capture the vibrational motion of the atoms accurately. For all the simulations, the crystal is first equilibrated at a baseline temperature, which is much lower than the melting point. It is then heated either continuously or in increments of 50 K at a rate of 0.01 K per time step (10^{13} K/s). For the latter case, each heating step is followed by an equilibration step of duration 50 ps. The equations of motions are numerically integrated using the Verlet algorithm. All MD simulations in this work are performed using the LAMMPS molecular dynamics package [13].

The melting point is identified by studying the variations in the potential energy, density, and mean square displacement. Density is determined by calculating the total mass of all atoms inside a fixed and predetermined volume. Mean square displacement is calculated as follows:

$$MSD = \frac{1}{N} \sum_{n=1}^N (\vec{r}(t) - \vec{r}(0))^2 \quad (2)$$

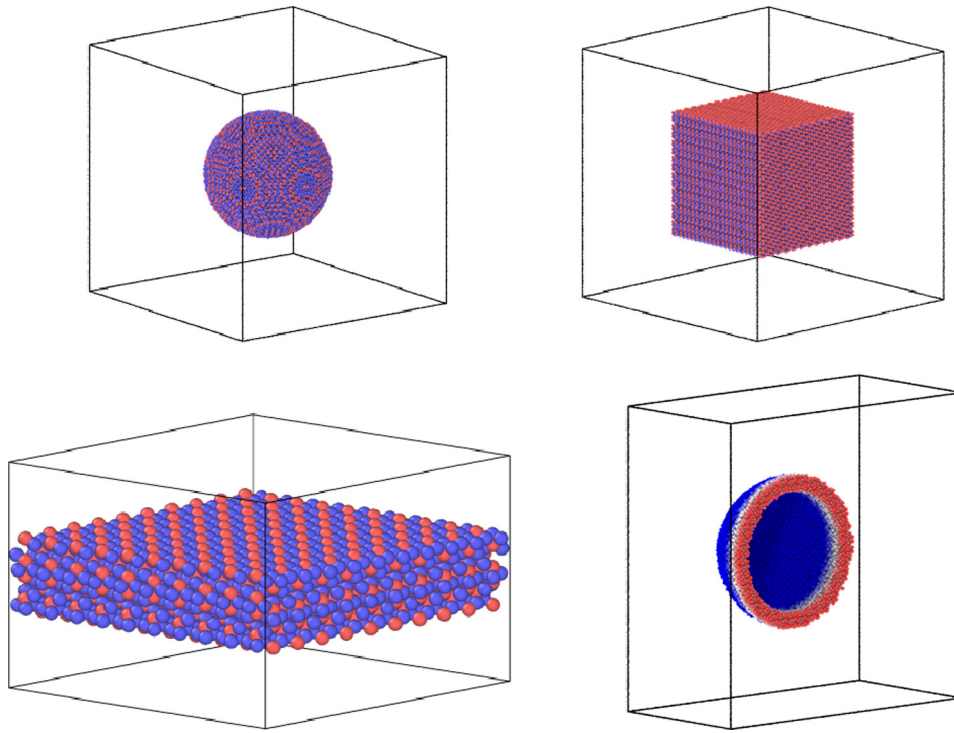


Fig. 1. Simulation domain and initial configuration used to study melting of (a) spherical particles; (b) cubic particles; (c) semi-infinite films; (d) spherical shells (dissected section is shown).

where r is the position vector and N number of atoms.

2.2. Thermodynamic analysis of melting

Melting temperatures are also calculated by means of thermodynamic analysis using the models of Gibbs-Thomson, Guisbiers et al.'s [14], and Qi et al.'s [15]. The Gibbs-Thomson model determines the melting point by equating the chemical potentials of solid and liquid nanoparticles ($\mu_s = \mu_l$). The resulting expression for the melting temperature is given by:

$$\frac{T_0 - T_m}{T_0} = \frac{2}{\rho_s r \Delta H_m} (\gamma_{sv} - \gamma_{lv}), \quad (3)$$

where T_m is the melting temperature of the nanocrystal, T_0 the bulk melting temperature, r the particle radius, ΔH_m the latent heat of melting, ρ_s the solid phase density, and γ the interfacial free energy. The subscripts s , l , and v denote the solid, liquid, and vapor phase, respectively.

Guisbiers et al.'s [14] model equates the Gibbs free energy of the liquid and solid nanocrystals and accounts for the changes in Gibbs

free energy due to the presence of free surfaces. The melting temperature can be calculated as follows:

$$\frac{T_0 - T_m}{T_0} = \frac{A}{\rho_s V \Delta H_m} (\gamma_{sv} - \gamma_{lv}) \quad (4)$$

where A/V is the surface area-to-volume ratio. Qi et al.'s [15] model, on the other hand, correlates the melting temperature with the cohesive energy and the following relation is obtained:

$$\frac{T_0 - T_m}{T_0} = \frac{n}{N}, \quad (5)$$

where $n = A/A_a$ is the number of interface atoms, A the surface area of nanocrystal, and A_a the area of an atom. The total number of atoms is given by $N = V/V_a$, where V is the volume of the nanocrystal and V_a atomic volume. The atomic radius is taken as 0.95 Å, based on the average Al–O bond length [16].

Eqs. (3)–(5) are used to calculate melting temperatures of nanocrystals for the case of homogeneous melting. It is, however, well known that melting of nanocrystals is a heterogeneous process, in which nucleation of the liquid phase occurs at the free surface [8]. As a result, liquid nucleation and growth (LNG) model is also considered in the present study [17]. LNG model assumes that the liquid phase nucleates at the free surface and the melting front propagates into the interior regions over time. The change in Gibbs free energy due to melt nucleation and growth can be expressed as follows:

$$\Delta G = V(G_V^L - G_V^S) + A_{sl} \gamma_{sl}, \quad (6)$$

where G is the Gibbs free energy, V the volume of the melted region, and A_{sl} the area of the solid-liquid interface. The heterogeneous nucleation of the melt phase poses a nucleation barrier, since an additional energy is required to create this interface. As a result, the Gibbs free energy may increase with increasing liquid shell thickness, depending on the temperature. Eq. (6) can be used to

Table 1
Parameters of the potential function developed by Vashishta et al. [12].

	Al	O		
$Z_i (e)$	1.5237	-1.0158		
$\lambda = 5.0 \text{ \AA}$	$\xi = 3.75 \text{ \AA}$	$r_c = 6.0 \text{ \AA}$	$e = 1.602 \times 10^{-19} \text{ C}$	
<i>Two body</i>				
η_{ij}	Al–Al	Al–O	O–O	
$H_{ij} (\text{eV \AA}^n)$	7	9	7	
$D_{ij} (\text{eV \AA}^4)$	12.7506	249.3108	564.7334	
$W_{ij} (\text{eV \AA}^6)$	0	50.1522	44.5797	
<i>Three body</i>				
	$B_{ijk} (\text{eV})$	$\bar{\theta}_{ijk} (\text{deg})$	C_{ijk}	$\gamma (\text{\AA})$
Al–O–Al	8.1149	109.47	10	1.0
O–Al–O	12.4844	90.0	10	1.0
				$r_0 (\text{\AA})$
				2.90

study the change in the Gibbs free energy and determine the melting point of nanocrystals.

2.3. Thermophysical property calculation

The thermophysical properties are important input parameters to the melting models. To compare MD simulation results with predictions of thermodynamics models, it is important to calculate these properties using MD simulations and feed them as input parameters to the thermodynamic melting models. There are four input parameters of concern: (1) bulk melting point, (2) latent heat of melting, (3) solid density, (4) solid and liquid surface free energies. As a part of the verification and validation process, the total energy per atom is calculated as a function of volume per atom. Calculations are performed using the energy minimisation technique with the help of the conjugate gradient algorithm. Fig. 2 shows the variation of total energy with volume on a per-atom basis. A good agreement between predictions of the present study and those of Vashishta et al. is observed. Note that the latter matches well with the Murnaghan equation of state [12].

2.3.1. Bulk melting point

Four different approaches have been adopted for determining the melting point of bulk alumina: (1) infinite crystal heating method; (2) semi-infinite crystal heating method; (3) solid-liquid coexistence simulations; and (4) thermodynamic method.

2.3.1.1. Infinite crystal heating method. NPT-MD simulations are carried out to determine the bulk melting point of alumina. The heating procedure is described in detail in Section 2.1. Periodic boundary conditions are imposed in all the three directions to simulate an infinite bulk crystal. Fig. 3 shows the variation of potential energy and density with temperature. Melting is characterized by a sudden change in density and potential energy, which is a characteristic of homogenous melting. Melting point can also be determined from the evolution of crystal structure and density profiles, as shown in Fig. 4. The entire crystal is divided into a number of bins along z direction and the number of atoms in each bin is counted. It is apparent that the calculated melting temperature is around 2850 K, significantly greater than the experimental value (~2350 K), indicating a superheating of about 20%. This can be attributed to the imposition of periodic boundary conditions in all directions and absence of nucleation of sites for melting. The latent heat of melting is calculated to be about 963 kJ/kg, which is comparable to the value of 1089 kJ/kg reported in the literature [18].

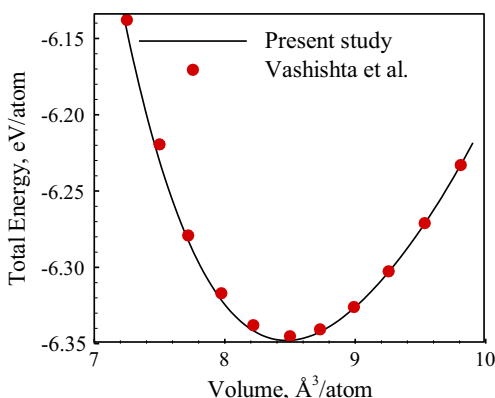


Fig. 2. Total energy per atom as a function of volume per atom: Comparison of results of the present study with those of Vashishta et al. [12].

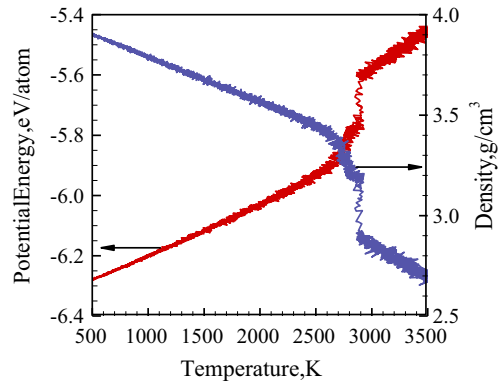


Fig. 3. Variation of potential energy per atom and density with temperature showing homogeneous melting of bulk alumina crystal at ~2850 K.

2.3.1.2. Semi-infinite crystal heating method. To circumvent the superheating issue and predict the heterogeneous melting point, a semi-infinite alumina crystal is considered. The procedure follows closely the approach described in Ref. [19]. A semi-infinite crystal of 34,260 atoms is first created and then heated continuously; the melting point is detected by studying the variation of the potential energy with temperature. To create a semi-infinite crystal, a set of few atomic layers at the bottom of the crystal are held fixed. However, the lattice constants obtained from NPT heating simulations of the infinite bulk are used to expand this region continuously in order to mimic the response of the bulk to heating. A free surface is created by exposing the upper surface of the crystal to vacuum and imposing reflecting boundary conditions. Fig. 5 shows the variation of the potential energy with temperature. As can be seen, the method predicts a heterogeneous melting point of ~2400 K, lower than the homogeneous melting point of ~2850 K obtained for the infinite bulk crystal.

2.3.1.3. Solid-liquid coexistence simulations. Another common approach to determine the bulk melting point is the solid-liquid coexistence simulations. In the present study, the procedure closely follows the approach described in detail in Refs. [20,21]. The length of the simulation box along the z direction is chosen to be greater than those along x and y directions to reduce phase boundary effect. The number of atoms in the crystal is 1920. The coexistence simulation involves four different stages. Fig. 6 shows the crystal snapshots and number of atoms in different bins along z direction for each stage. The entire crystal is divided into number of bins of length 1 Å along z direction and number of atoms in each bin is counted. In the first stage, NPT-MD simulations are conducted to heat the crystal to a temperature close to the expected melting point (T_1). For the case shown in Fig. 6, the temperature (T_1) is 2200 K. The resulting crystal is then used as the starting configuration for the second stage. The crystal is divided into two groups: A1 (the left half) and A2 (the right half). Positions and velocities of the atoms in the A1 group are fixed, while atoms of the A2 group are heated to a temperature (T_2) beyond the melting point using an anisotropic Nosé–Hoover thermostat-barostat ($NP_{zz}T$). The external pressure along z direction is equal to the initial pressure (P_1). This approach is taken so that the crystal dimensions along x and y directions are unchanged. From the figure, it is apparent that the A2 crystal has melted. During the third stage, A2 region is suddenly cooled in $NP_{zz}T$ ensemble to the initial temperature (T_1) at a high cooling rate such that crystallization does not occur. In the fourth stage, atoms of the A1 group are no longer fixed and the entire crystal is equilibrated at the initial temperature (T_1) and initial pressure (P_1) using the Nosé–Hoover thermostat-

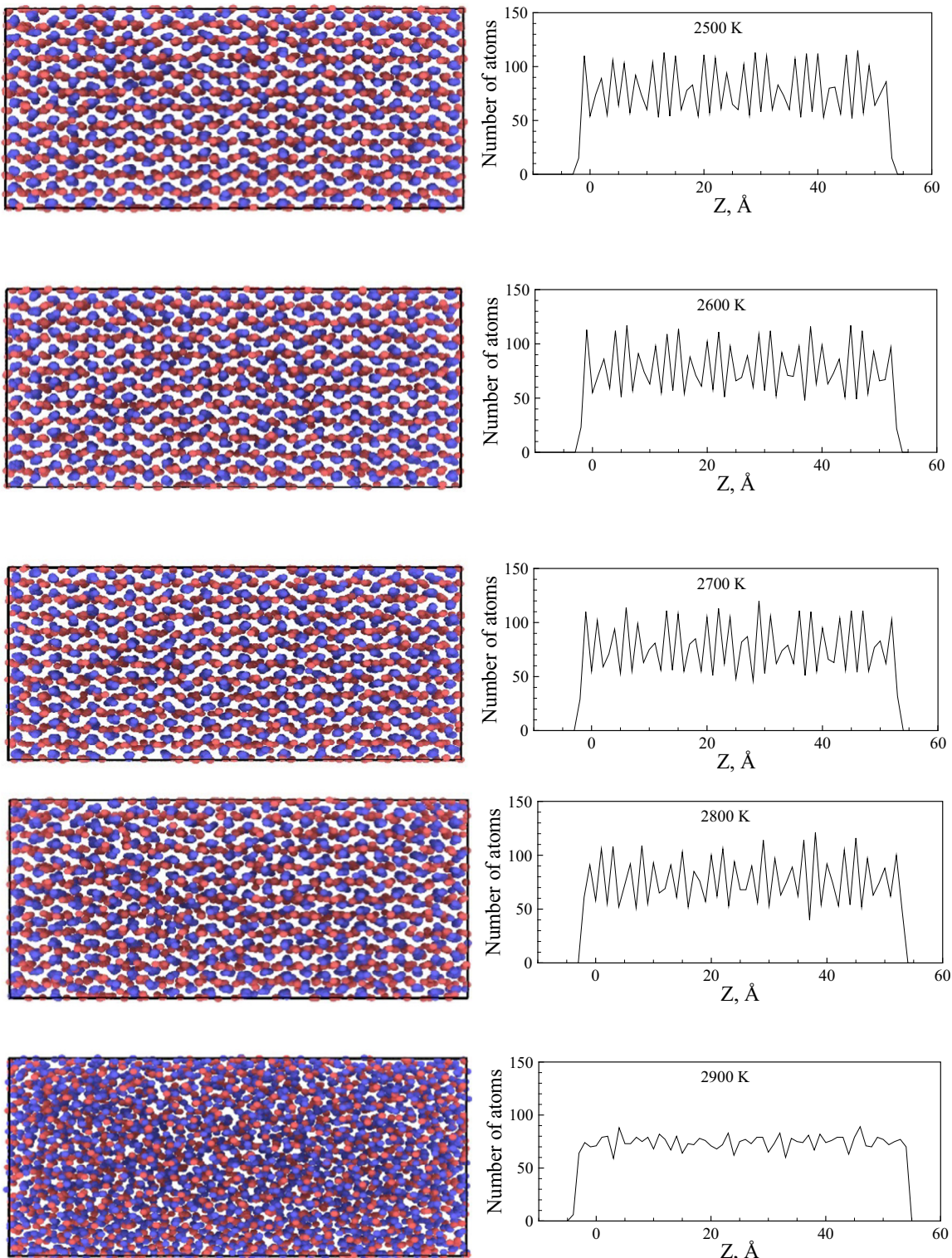


Fig. 4. Evolution of crystal structure and number atoms in different bins during heating of an infinite bulk alumina crystal.

barostat. If the entire crystal solidifies during the fourth stage, it is apparent that the chosen temperature (T_1) is lower than the melting point. This is the situation for the case of 2200 K shown in Fig. 6. On the other hand, if the entire crystal melts during the fourth stage, it is obvious that the chosen temperature (T_1) is greater than the melting point. This is the situation for the case of 2600 K shown in Fig. 7. By doing a series of such calculations,

the melting point of bulk alumina is calculated to be ~ 2500 K. A similar study in which melting point predictions of solid-liquid coexistence simulations are compared with those of infinite crystal heating method for corundum [22]. The melting point obtained using the latter method is 2425–2475 K, substantially greater than the prediction of coexistence simulations (2200 K). Note, however, that Matsui potential function was employed in that study.

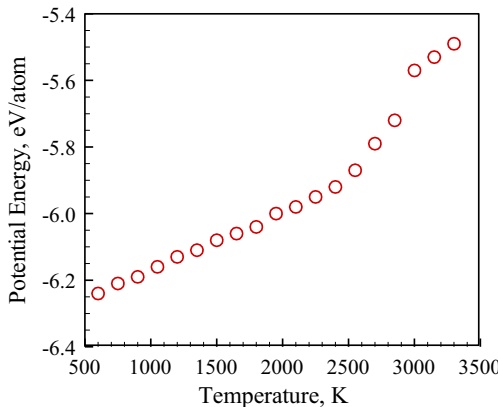


Fig. 5. Variation of potential energy of a semi-infinite alumina crystal with temperature showing heterogeneous melting at ~2400 K.

2.3.1.4. Thermodynamic method. The melting point is also determined by calculating the Gibbs free energy of solid and liquid phases and determining the temperature at which they are equal. **2.3.1.4.1. Bulk solid free energy calculation.** The free energy per atom of the alumina crystal is obtained using the thermodynamic integration approach with a suitable reference system [23]. The free energy of the actual system per atom is given by

$$g_2(T_0, P = 0) = g_1(T_0) + \Delta g_1, \quad (7)$$

where g_2 and g_1 are the free energies per atom of the actual and reference systems, respectively. The difference, Δg_1 , is computed as follows:

$$\Delta g_1(P = 0) = \frac{1}{N} \int_0^1 \left\langle \frac{\partial H}{\partial \lambda} \right\rangle_{\lambda} d\lambda = \frac{1}{N} \int_0^1 \langle U_2 - U_1 \rangle d\lambda, \quad (8)$$

where λ is the coupling constant (which is varied from 0 to 1), H is the parametric Hamiltonian ($H = \lambda H_1 + (1-\lambda)H_2$), U the potential energy and N the number of atoms. The integral is evaluated using the non-equilibrium Frenkel-ladd approach [24]:

$$\frac{1}{N} \int_0^1 \langle U_2 - U_1 \rangle d\lambda = \frac{1}{2} (w_{\text{irr}}^{2 \rightarrow 1} - w_{\text{irr}}^{1 \rightarrow 2}), \quad (9)$$

where the irreversible work done, $w_{\text{irr}}^{a \rightarrow b}$, is given by:

$$w_{\text{irr}}^{a \rightarrow b} = \frac{1}{N} \int_0^{t_s} dt \left(\frac{d\lambda}{dt} \right) \langle U_a - U_b \rangle_{\lambda}, \quad (10)$$

where t_s is the switching time, U_1 and U_2 represents the potentials for the reference and actual systems, respectively, for a given set of MD atomic positions. For the actual system, the Vashishta potential is used and the reference system is taken as an Einstein crystal with the spring constants estimated from the mean square displacements:

$$k_{\text{Al}/0} = \frac{3k_B T_0}{\langle (r - r_0)^2 \rangle_{\text{Al}/0}}, \quad (11)$$

where k_B the Boltzmann constant, r the position vector, and r_0 the reference lattice position of the atom. The free energy per atom for an Einstein crystal is given by:

$$g_1 = \frac{-3k_B T_0}{N} \left(N_{\text{Al}} \ln \left(\frac{2\pi k_B T_0}{h\omega_{\text{Al}}} \right) + N_0 \ln \left(\frac{2\pi k_B T_0}{h\omega_0} \right) \right) \quad (12)$$

where h is the Planck's constant, N the total number of atoms in the simulation domain, and ω the angular frequency. The angular frequency is obtained from the spring constants. To calculate the free energy, a system of 2160 atoms is considered and periodic boundary conditions are enforced in all three directions. The crystal is

heated at constant pressure to the desired temperature using a Langevin thermostat. The obtained crystal is equilibrated for 50,000 timesteps. The springs constants are calculated using the mean square displacement values obtained in the last 20,000 timesteps of the equilibration stage. For the Frenkel Ladd path, a switching time of 100,000 timesteps and an equilibrium step of 50,000 time steps has been employed. Fig. 8 shows the variation of the integrand, $\langle U_a - U_b \rangle_{\lambda}/N$, with the coupling constant during the switching process.

2.3.1.4.2. Bulk liquid free energy calculation. The procedure for calculating the free energy of bulk liquid closely follows the approach described in Ref. [25]. The reference system can be taken as the ideal gas mixture with the same density and temperature as the original system. However, this may result in unphysical results. As a result, the reference system is taken to be a purely repulsive gas. The free energy of liquid alumina per atom is thus calculated as follows:

$$g_{\text{liquid}} = g_{\text{repulsive}} + \Delta g_1. \quad (13)$$

$$g_{\text{repulsive}} = g_{\text{ideal gas}} + \Delta g_2. \quad (14)$$

In order to determine Δg_1 , switching is performed from the liquid phase into a purely repulsive gas with the following potential:

$$U_{\text{repulsive}} = 0.1 \left(E_{\text{vashishtha}}^{\text{pair repulsive}} \right). \quad (15)$$

The procedure to calculate the difference, Δg_1 , is similar to that of solids, with the exception that only the forward path is used. As shown in Eq. (14), the free energy of the repulsive gas is determined by slowly expanding the purely repulsive gas from the initial density to ideal gas limit ($\rho \rightarrow 0$) and then compressing it to the initial density. The analytical expression for the change in free energy during the expansion-compression process is given by:

$$\Delta g_2 = k_B T \int_0^{\rho_0} \left[\left(\frac{P}{\rho k_B T} \right) - 1 \right] \frac{d\rho}{\rho}, \quad (16)$$

where ρ_0 is the initial density of the repulsive gas, and P and ρ are determined during the expansion stage. The free energy of the ideal gas is calculated using the following expression:

$$g_{\text{ideal gas}} = \frac{1}{N} \left(k_B T_0 [N_{\text{Al}} (\ln(\rho_0 \Lambda_{\text{Al}}^3) - 1) + N_0 (\ln(\rho_0 \Lambda_0^3) - 1)] \right), \quad (17)$$

where Λ is the DeBroglie wavelength of the ideal gas:

$$\Lambda_{\text{Al}/0} = \frac{h}{\sqrt{2\pi m_{\text{Al}/0} k_B T_0}} \quad (18)$$

The bulk alumina is first heated in an NPT ensemble to the desired temperature. The sample is then slowly converted to a repulsive gas over a time period of 100,000 timesteps. Once the repulsive gas is obtained, it is expanded in stages and the statistics needed for evaluating the integral in Eq. (16) are collected. A second order polynomial, obtained by curve fitting the data points, is then used to numerically evaluate the integral.

Fig. 9 shows the dependence of Gibbs free energy on temperature for solid and liquid alumina. It is apparent that the two curves intersect at a temperature of 2450 K. As the melting points obtained by different methods are in the range of 2400–2500 K, a melting point value of 2450 K is used in the thermodynamic analysis of melting. This is noticeably greater than the experimental value of 2350 K, suggesting that the potential function overpredicts the melting point.

2.3.2. Density of solid alumina

Density of solid alumina is another important property of concern and it is a function of temperature. In the present study, density of bulk solid alumina is calculated using NPT MD simulations.

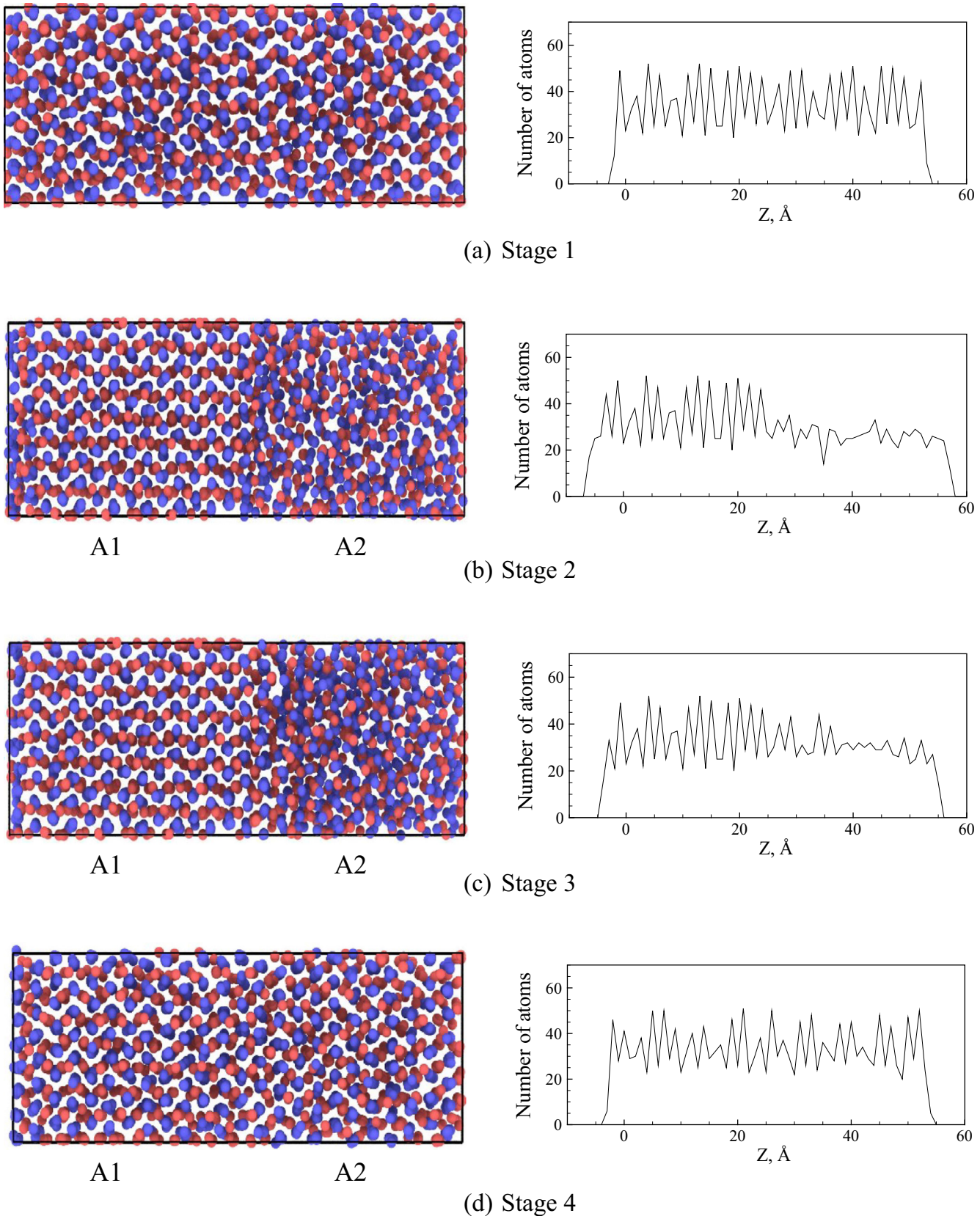


Fig. 6. Evolution of crystal structure and number of atoms in different bins during solid-liquid coexistence simulation at a temperature of 2200 K.

Fig. 10 shows the variation of density of solid alumina with temperature. A curve fit to the MD simulation data is performed to obtain an equation for the temperature dependence of the density

of solid alumina, which is used as an input to the thermodynamic analysis of melting. Comparison is also drawn with the data reported by Akshay et al. [26], which is consistent with the data

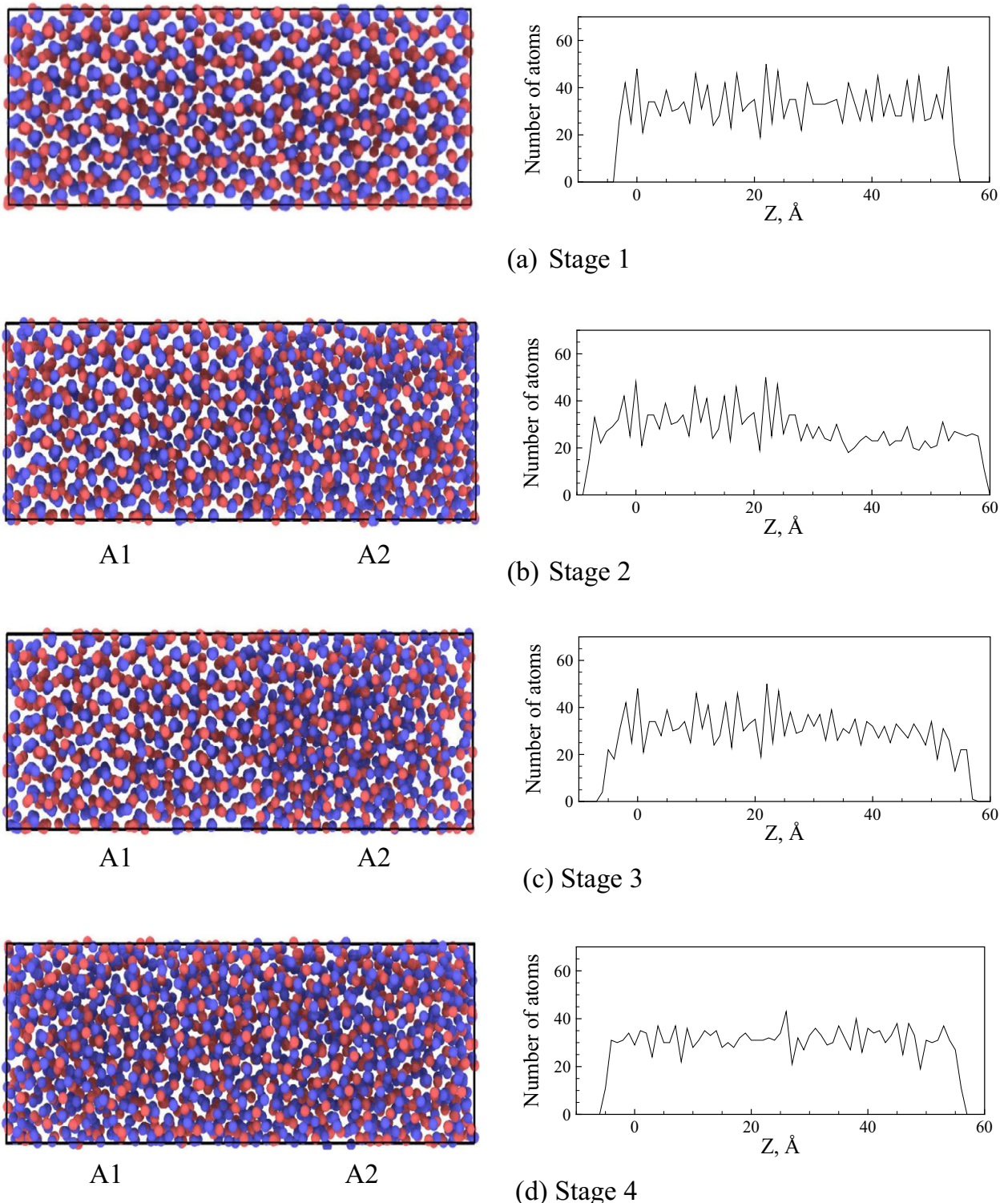


Fig. 7. Evolution of crystal structure and number of atoms in different bins during solid-liquid coexistence simulation at a temperature of 2600 K.

of Turnay [27], Levitas et al. [28], and Paradis et al. [29]. In Ref. [26], the following equation for solid alumina density is proposed:

$$\rho_s = 4.002 - (1.083 \times 10^{-4})(T - 237) \quad (19)$$

where ρ_s is the density of solid alumina and T is the temperature. For the sake of comparison, Eq. (19) is also used in the thermodynamic analysis.

2.3.3. Surface free energy

Surface free energy is another input parameter in the thermodynamic melting analysis. For solid alumina, surface free energy is calculated as follows:

$$\gamma_s = \frac{N(g_{\text{slab}} - g_{\text{bulk}})}{2A_s}, \quad (20)$$

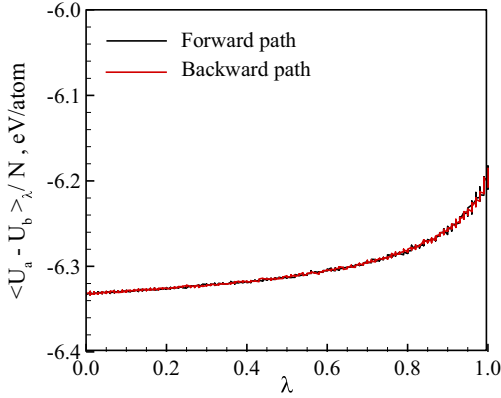


Fig. 8. Variation of $\langle U_a - U_b \rangle_{\lambda}/N$ with coupling constant, λ , for forward and backward paths a temperature of 300 K.

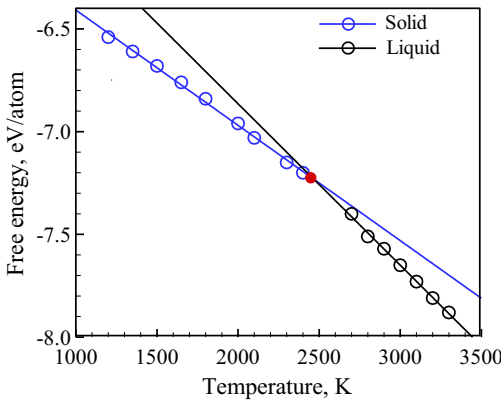


Fig. 9. Variation of free energy of bulk solid and liquid alumina with temperature obtained using MD simulations.

where g_{bulk} and g_{slab} are the calculated free energies of the bulk and the slab. Surface free energy is calculated by conducting constant volume and temperature MD simulations. The solid slabs are prepared using the NPT lattice constants obtained from the bulk simulations. The created surface is relaxed before calculating the free energy. Calculations are performed for (0 0 1), (0 1 0), and (1 0 0) planes.

For liquids, the surface free energy/surface tension is calculated as follows:

$$\sigma = \frac{l_n}{2} \langle p_n - p_t \rangle \quad (21)$$

where p is the pressure and l_n the length of the simulation domain in the normal direction. The subscripts n and t refer to normal and tangential directions. Surface tension for liquid alumina is calculated over a temperature range of 2800–3400 K. The liquid alumina slab is created by adding vacuum on both sides and the slab is then equilibrated in a NVT ensemble for 600,000 timesteps. To obtain the statistics, data is collected for 400,000 timesteps. Fig. 11 shows the surface free energy of solid and liquid alumina for different temperatures. Comparison with data available in the literature is also shown. Surface tension of liquid alumina is taken from Ref. [18], which are compared with the experimental data of Kingery [30], Bartlett et al. [31], Rasmussen et al. [32] and Wartemberg et al. [33]. As can be seen, the calculated surface tension values agree reasonably well with reported data. For solids, the surface free energy appears to be dependent on the orientation of the free surface. In addition to the values obtained using MD simulations, the equation reported in Ref. [34] is used. Note that the Frenkel-ladd approach

becomes less suitable to estimate surface free energies of [1 0 0] and [0 1 0] surfaces at high temperatures due to configurational disorders [35]. As a result, calculations are performed only up to a tem-

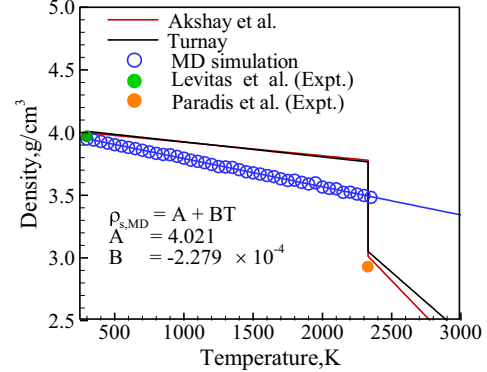


Fig. 10. Variation of density of alumina with temperature: comparison of predictions of MD simulations with data available in the literature. The solid and liquid densities are taken from Refs. [26] and [27], which are compared with the experimental data of Levitas et al. [28] and Paradis et al. [29].

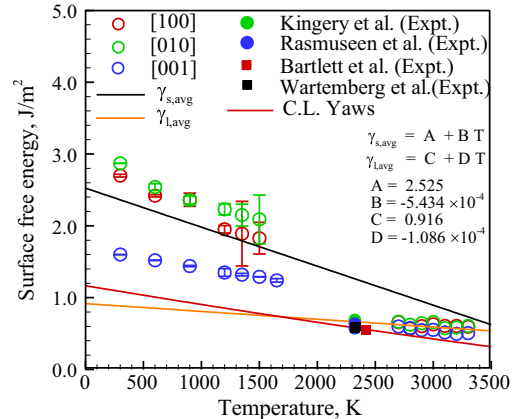


Fig. 11. Variation of surface free energy of solid and liquid alumina with temperature: comparison of MD simulation predictions with values in the literature. Surface tension of liquid alumina is taken from Ref. [18], which are compared with the experimental data of Kingery [30], Bartlett et al. [31], Rasmussen et al. [32] and Wartemberg et al. [33]. Error bars indicate dissipative errors in Frenkel-Ladd approach.

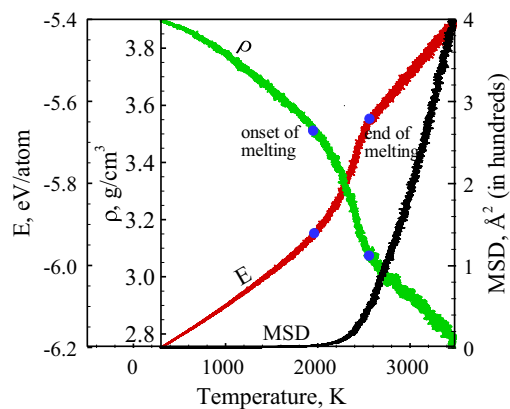


Fig. 12. Variations of potential energy (E), density (ρ) and mean square displacement (MSD) with temperature for a 6 nm spherical alumina particle: continuous heating method.

perature of 1650 K and a curve-fit to these data points is used to estimate high-temperature values of solid surface free energies. In future works, alternative strategies can be adopted to estimate the magnitude of error resulting from such an extrapolation and come up with more accurate high-temperature estimates of surface free energies. Note that the [0 0 1] plane is less susceptible to such configurational disorders, as indicated by the error bars in Fig. 11.

3. Results and discussion

After model validation, MD simulations are performed to study melting of alumina nanocrystals. Fig. 12 shows the variations of the potential energy, density, and mean square displacement (MSD) for a 6 nm spherical particle. The onset and completion points of melting are indicated in the figure. Properties are initially essentially constant or vary linearly with temperature. As the temperature reaches around 1950 K properties start to deviate substantially from the initial trend. The melting point is thus identified to be 1950 K for a particle diameter of 6 nm. Melting mechanism is also studied by monitoring the evolution of thermal displacement of atoms. The atomic thermal displacement is given by:

$$\delta_{t,i} = \sqrt{(r_i - r_{0,i})^2}, \quad (22)$$

where r is the position vector. The subscripts i and 0 refer to atom i and the initial state.

Fig. 13 shows the snapshots of the crystals at different temperatures. It is apparent that melting is a heterogeneous process in which the nucleation of the liquid phase begins at the outer surface (exposed to vacuum) and the melting front propagates into the interior regions with increasing temperature. Free surfaces act as nucleation sites for heterogeneous melting and melting takes place gradually over a range of temperatures.

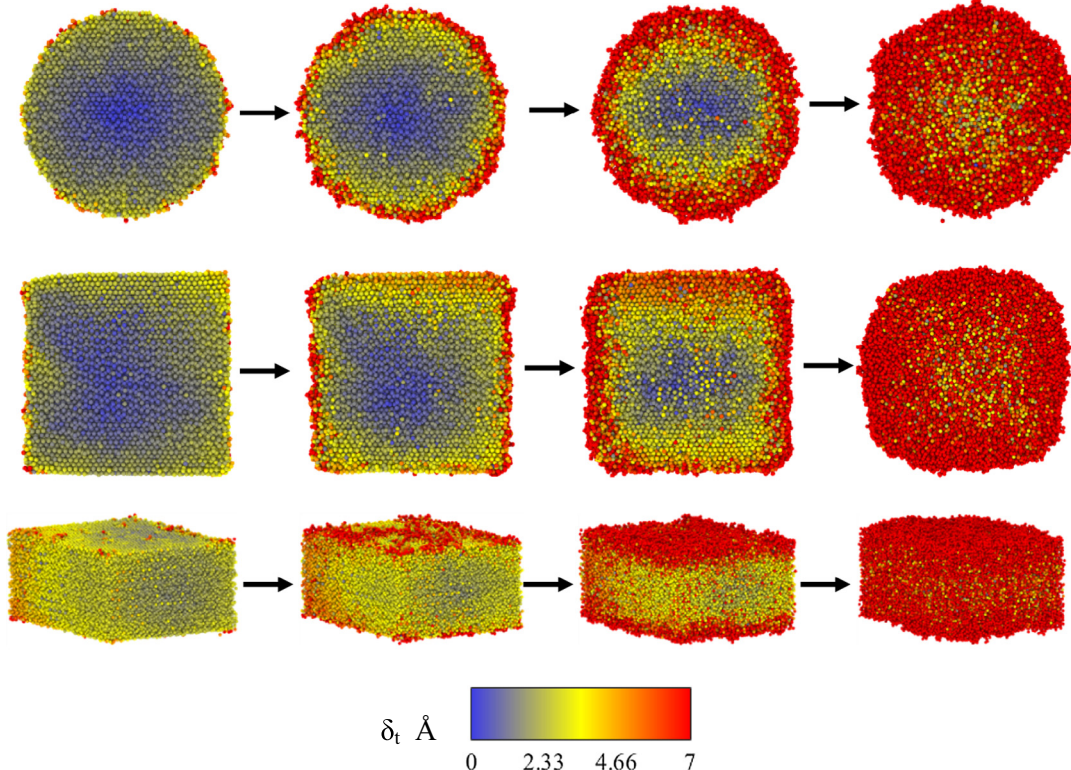


Fig. 13. Snapshots of Al_2O_3 nanocrystals colored by thermal displacement of atoms for three different cases: (A) 10 nm spherical particle (B) 10 nm cubic particle (C) 6.49 nm thick semi-infinite film.

3.1. Melting of spherical and cubic alumina nanocrystals

Melting of spherical and cubic nanocrystals is first explored. Fig. 14 shows the size effect on the melting temperatures of spherical and cubic particles. MD simulation results are compared with predictions of thermodynamic melting models (based on both MD derived and reported thermophysical properties). The melting points of spherical and cubic particles are nearly the same; this is not surprising considering similar surface-area-to-volume ratios. MD results suggest that the melting point drops sharply below a threshold particle size, which is 4 nm for spherical and cubic particles. Beyond 4 nm, crystal size exerts a weak effect on the melting point. The thermodynamic models qualitatively capture the size effect on the melting point, although there are significant variations based on differences in the property values and the choice of the model. Qi et al. [15] model, which is based on fraction of surface atoms in the crystal, predicts the highest melting points among the models considered. The Gibbs-Thompson model predicts higher melting points than the Guisbiers et al. model. This is apparent from Eqs. (3) and (4), considering the fact that the surface-area-to-volume ratio (A/V) of spherical particles is $3/r$, where r is the particle radius. When temperature-dependent properties are used, a lower melting temperature is predicted. This is because the depression in the melting point is directly proportional to the difference in surface free energies ($\gamma_{sv} - \gamma_{lv}$), which increases with decreasing temperature.

Melting point is also determined using the liquid nucleation and growth (LNG) model considering the heterogeneous melting mechanism. Fig. 15 shows the variation of the Gibbs free energy with shell thickness for a 10 nm spherical alumina particle. For temperatures lower than the melting temperature predicted by Guisbiers et al. model (2147 K), Gibbs free energy change is always positive and the Gibbs free energy of a completely liquid particle (corre-

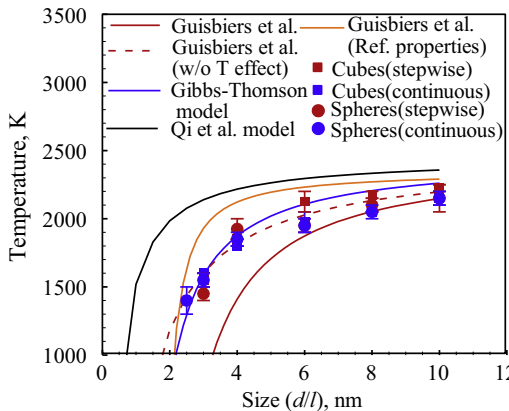


Fig. 14. Melting temperatures of cubic and spherical particles as a function of their size (l : cube edge length and d : particle diameter) determined by MD simulations and thermodynamic melting models.

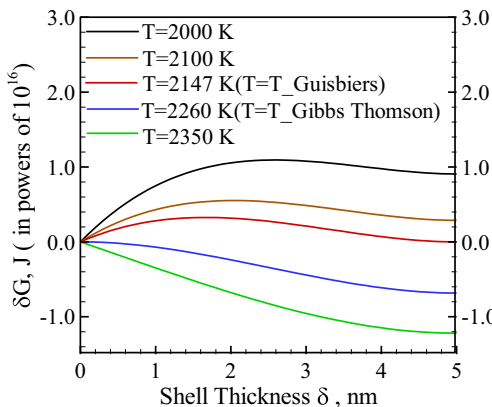


Fig. 15. Variation of Gibbs free energy with shell thickness for a 10 nm spherical alumina particle for different temperatures.

sponding to $\delta = 5$ nm) is greater than that of a completely solid particle. As a result, melting is not thermodynamically favourable. At 2147 K, the Gibbs free energy change is zero for a shell thickness of 5 nm, suggesting the possibility of homogenous melting. The melting point predicted by Guisbiers et al. model can thus be regarded as the lower limit of the LNG model, as no solid-liquid interface is formed. As the temperature increases to the melting point predicted by the Gibbs-Thomson model (2260 K), the Gibbs free energy change monotonically decreases with increasing shell thickness, representing a spontaneous phase transformation. As a result, melting point predicted by the Gibbs-Thomson model can be regarded as the upper limit of the LNG model.

3.2. Melting of planar alumina films

Melting of semi-infinite planar alumina films is then explored and emphasis is again placed on the size effect on the melting temperature. Fig. 16 shows the predictions of MD simulations and thermodynamic melting models. The melting points of planar semi-infinite films are greater than those of spherical and cubic particles, especially for thinner films, because of lower surface-area-to-volume ratios. As with spherical and cubic particles, results suggest that the melting point drops sharply below a threshold particle size, which is about 2 nm for semi-infinite planar films. Note that the melting points predicted by Dreizin et al. [11] are lower than the predictions of this work, suggesting the possibility

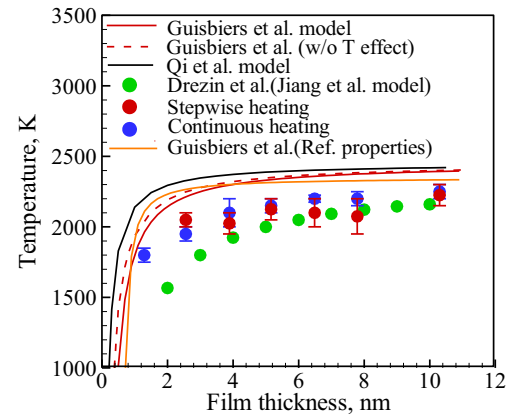


Fig. 16. Melting temperature of semi-infinite films as a function of thickness as predicted by MD simulations and equilibrium melting models. Predictions are also compared with the values obtained by Dreizin et al. [11].

that Jiang et al.'s model overestimates the melting point depression for thin films.

The previous analysis considered semi-infinite films, which are infinite in two directions. In reality, flake Al particles and planar Al substrates (and their oxides films) are of finite length (as shown in Fig. 17). As a result, the presence of free surface in the lateral directions must also be considered. To estimate the melting point, Guisbiers et al. model is used since it has reasonably captured the size effect on melting point. Fig. 18 shows the variation of melting point of finite films with film thickness for different film lengths. The melting point of the film increases with the film length due to a reduction in the surface area-to-volume ratio. The melting points are nearly equal to those of a semi-infinite planar film for a film length of 1 μ m. Semi-infinite treatment is thus justifiable for sufficiently long films ($l > 1 \mu\text{m}$).

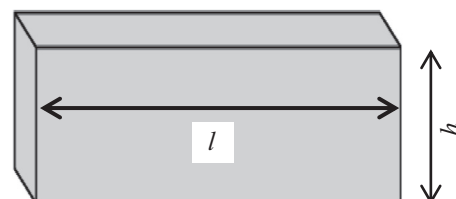


Fig. 17. Schematic illustrating a finite planar film; l is the length and h the height of film.

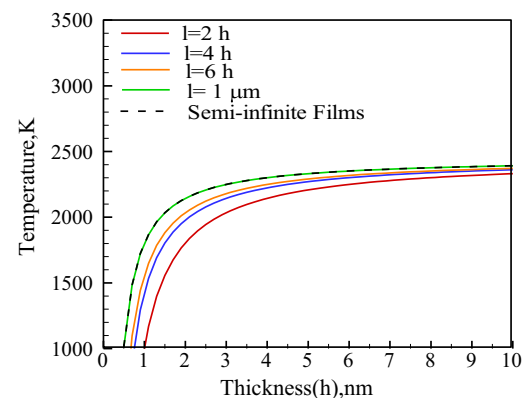


Fig. 18. Variation of melting point of finite planar films with film thickness for different film lengths.

3.3. Melting of spherical alumina shells

It is not immediately apparent if the results obtained for planar films are applicable for spherical alumina shells. Firstly, curvature effects could become important, especially at nano-scales. For planar films, the film thickness is the only parameter that affects the melting point. For spherical shells, both oxide film thickness and Al core diameter could influence the melting point. For all these reasons, spherical alumina shells must be considered, as shown in Fig. 19. Here, both inner and outer surfaces are first treated as free surfaces (case A). The melting point of the spherical alumina shell is determined using the Guisbiers et al. model:

$$T_m = T_o \left(1 - \left(\frac{A_o + A_i}{V} \right) \frac{(\gamma_s - \gamma_L)}{\rho_s \Delta H_m} \right), \quad (23)$$

$$\frac{A_o + A_i}{V} = \frac{6(d_o^2 + d_i^2)}{d_o^3 - d_i^3}, \quad (24)$$

where d_o is the outer diameter and d_i the inner core diameter. Note that the inner surface is strictly not a free surface due to the presence of the aluminum core. One of the major uncertainties is the Al-Al₂O₃ interfacial energy (and its temperature dependence). Due to the unavailability of reliable data, melting point is also determined by ignoring the core-shell interfacial energy and assuming that energy of the interfacial atoms is same as that of the bulk (case B). Under this simplification, the melting point expression takes the form:

$$T_m = T_o \left(1 - \frac{A_o(\gamma_s - \gamma_L)}{V \rho_s \Delta H_m} \right), \quad (25)$$

$$\frac{A_o}{V} = \frac{6d_o^2}{d_o^3 - d_i^3}, \quad (26)$$

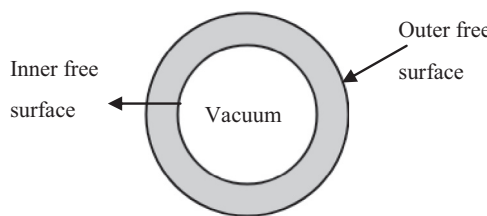
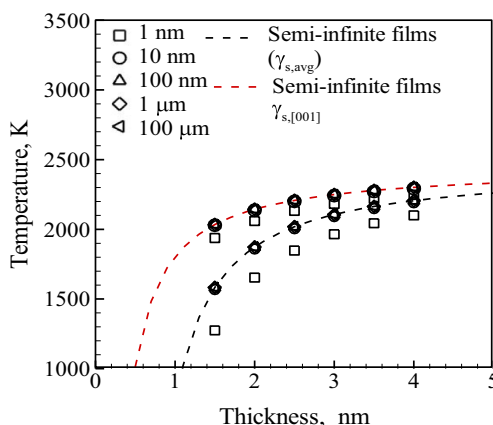


Fig. 19. Schematic of a spherical alumina shell for which both the inner and outer surfaces are regarded as free surfaces (case A).



where d_o is the outer diameter and d_i the inner core diameter. Fig. 20 shows the comparison of melting temperatures of spherical alumina shells for the two cases with those of semi-infinite alumina films. For core diameters greater than 10 nm (or few tens of nm), the melting points of spherical shells are nearly the same as those of semi-infinite planar films. Below 10 nm (or few tens of nm), curvature effects become important and the difference in the melting points of the two geometries becomes substantial, especially for thinner films. As particle size range of concern is typically of the order of or greater than 100 nm, semi-infinite planar film approximation appears to be reasonable to estimate the melting point of spherical alumina shells. A related observation is that the shell melting point is essentially independent of core size beyond 10 nm (or few tens of nm). As a result, the melting point of the oxide shell encapsulating a 100 nm aluminum particle is about the same as that of a 100 μm particle. It is not surprising that the predictions of the model are quite sensitive to choose of surface free energy values.

Fig. 21 shows the comparison of the calculated melting points of spherical alumina shell with those reported in the literature. In case A, both inner and outer surfaces are treated as free surfaces, whereas in case B, the core-shell interfacial energy is ignored. Case B predicts higher melting points than case A for obvious reasons. The difference becomes more pronounced for thinner shells and is substantial for a shell thickness of 1 nm. Predictions of MD sim-

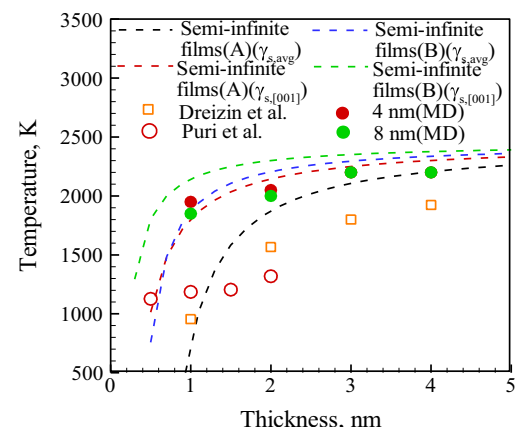


Fig. 21. Melting point of spherical alumina shell as a function of thickness for different core diameters: (A) both inner and outer surfaces are treated as free surfaces; (B) core-shell interfacial energy is ignored. MD results are shown for two core diameters 4 nm and 8 nm. Comparison with the results of Dreizin et al. [11] and Puri et al. [10] is also shown.

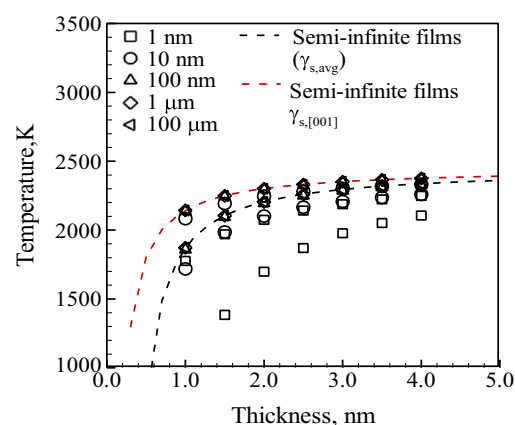


Fig. 20. Comparison of melting temperatures of spherical alumina shells with semi-infinite alumina films for (a) two free surfaces; (b) one free surface.

ulations and thermodynamic melting models do indicate that the melting point of 2–4 nm oxide layers passivating Al particles is not a strong function of core size and shell thickness and vary roughly between 1800 K and 2350 K. Results of the present study is different from those of the previous works ([10,11]), where a more substantial depression of melting point was reported. This raises concerns about the validity of the potential function and thermodynamic models used in the previous works. Another important implication of the present study is that the melting point depression of nano-scale alumina films does not explain the observed scatter in the ignition temperature of aluminum particles. The measured ignition temperatures vary in the range of 1000–2350 K, whereas oxide layer melting points obtained in this work are in the range of 1800–2350 K. This implies that additional physicochemical processes and mechanisms such as core melting and polymorphic phase transformations must be considered to describe ignition of aluminum particles. Note that the present study considered only alpha alumina crystals, while it is well known that other alumina polymorphs such as gamma and amorphous alumina exist. Melting of these phases can be studied as a part of future studies.

4. Conclusions

Molecular dynamics (MD) simulations and thermodynamic analysis are conducted to investigate the size effect on melting point of alumina nanocrystals. Different geometries including spherical and cubic particles, planar thin films, and spherical shells are considered. In MD simulations, the atomic interactions are captured using Vashishta et al.'s potential function. A number of thermodynamic melting models, including both homogeneous and heterogeneous melting models, are considered. Thermophysical properties of concern to melting are calculated using MD simulations and are fed as inputs to thermodynamic melting models. Predictions of MD simulations are compared with those of thermodynamic melting models. Following are the main conclusions of the present study:

- For all cases, heterogeneous melting is observed, in which the nucleation of the melt phase occurred at the free surface and the melting front propagated into the interior regions of the crystal with time.
- MD results suggest that the melting point drops sharply below a threshold particle size, which is about 4 nm for spherical/cubic particles and about 2 nm for semi-infinite planar films.
- Semi-infinite treatment is justifiable for sufficiently long films. Melting points of finite planar films are nearly the same as those of semi-infinite counterparts, provided the film lengths are greater than $\sim 1 \mu\text{m}$.
- Semi-infinite planar films also offer reasonable estimates of melting points of spherical shells (with two free surfaces), provided core sizes are larger than 10 nm.
- For particle sizes of practical concern (greater or equal to 100 nm), melting points of 2–4 nm thick spherical oxide shells vary in the range of about 1800–2350 K, which is relatively near the bulk melting point. An enormous depression in the melting point is thus not observed.
- The oxide shell melting point is independent of core size beyond 10 nm (or few tens of nm). This implies that the melting point of the alumina shell encapsulating 100 nm and 100 μm particles are essentially the same. At nano-scales, the core size does not cause an additional “nano effect”, unless the size is extremely small.
- Predictions of thermodynamic melting models are in qualitative agreement with MD simulation results. Both Gibbs-Thomson

and Guisbiers et al. models predict the size dependence of melting point of nanocrystals reasonably well. Gibbs-Thomson and Guisbiers et al. models represent the upper and lower limits of the heterogeneous liquid nucleation and growth melting model, respectively. Treatment of temperature dependence of properties results in a greater melting point depression. Model predictions are quite sensitive to the thermophysical property values.

- Results of the present study suggest that the depression of melting point of the oxide layer cannot fully explain the existing scatter in the ignition temperature of aluminum particles. Other theories such as Al core melting and polymorphic phase transformations in the oxide layer must be considered.

Acknowledgements

This work is financially supported in part by the Research Initiation and Internal Research Grants provided by Indian Institute of Technology Gandhinagar (IITGN). We also acknowledge the fellowship provided by Ministry of Human Resource Development (MHRD), Government of India, through IIT Gandhinagar to the M. Tech. students, Nikhil Joshi and Nilkumar Mathur. The Junior Research Fellowship of Tejas Mane is financially supported by the Science and Engineering Research Board (SERB), India, through the Early Career Research Award to the corresponding author (D.S. Sundaram). The authors also acknowledge the efforts and support rendered by Ms. Pooja Bhat, Junior Research Fellow, IIT Gandhinagar. The authors thank Information System Technology Facility (ISTF) and High Performance Computing (HPC) team of IITGN for their help and support.

References

- [1] D.S. Sundaram, V. Yang, V.E. Zarko, Combustion of nano aluminum particles (Review), *Combust. Explos. Shock Waves*. 51 (2015) 173–196, <https://doi.org/10.1134/S0010508215020045>.
- [2] L.P.H. Jeurgens, W.G. Sloof, F.D. Tichelaar, E.J. Mittemeijer, Growth kinetics and mechanisms of aluminum-oxide films formed by thermal oxidation of aluminum, *J. Appl. Phys.* 92 (2002) 1649–1656, <https://doi.org/10.1063/1.1491591>.
- [3] J. Sanchez-Lopez, Passivation of nanocrystalline Al prepared by the gas phase condensation method: An x-ray photoelectron spectroscopy study, *J. Mater.* 13 (1998) 703–710.
- [4] R. Friedman, A. Maćek, Ignition and combustion of aluminium particles in hot ambient gases, *Combust. Flame*. 6 (1962) 9–19.
- [5] V.I. Rozenband, N.I. Vaganova, A strength model of heterogeneous ignition of metal particles, *Combust. Flame*. 88 (1992) 113–118, [https://doi.org/10.1016/0010-2180\(92\)90011-D](https://doi.org/10.1016/0010-2180(92)90011-D).
- [6] A. Rai, K. Park, L. Zhou, M.R. Zachariah, Understanding the mechanism of aluminium nanoparticle oxidation, *Combust. Theory Model.* 10 (2006) 843–859, <https://doi.org/10.1080/13647830600800686>.
- [7] M.A. Trunov, M. Schoenitz, E.L. Dreizin, Effect of polymorphic phase transformations in alumina layer on ignition of aluminium particles, *Combust. Theory Model.* 10 (2006) 603–623, <https://doi.org/10.1080/13647830600578506>.
- [8] Q.S. Mei, K. Lu, Melting and superheating of crystalline solids: From bulk to nanocrystals, *Prog. Mater. Sci.* 52 (2007) 1175–1262, <https://doi.org/10.1016/j.pmatsci.2007.01.001>.
- [9] R.F. Geller, P.J. Yavorsky, Melting point of alpha-alumina, *J. Res. Natl. Bur. Stand.* 34 (1945) 395–401.
- [10] P. Puri, V. Yang, Thermo-mechanical behavior of nano aluminum particles with oxide layers during melting, *J. Nanoparticle Res.* 12 (2010) 2989–3002, <https://doi.org/10.1007/s11051-010-9889-2>.
- [11] E. Dreizin, D. Allen, N. Glumac, Depression of melting point for protective aluminum oxide films, *Chem. Phys. Lett.* 618 (2015) 63–65.
- [12] P. Vashishta, R.K. Kalia, A. Nakano, J.P. Rino, Interaction potentials for alumina and molecular dynamics simulations of amorphous and liquid alumina, *J. Appl. Phys.* 103 (2008) 83504, <https://doi.org/10.1063/1.2901171>.
- [13] S. Plimpton, Fast parallel algorithms for short-range molecular dynamics, *J. Comput. Phys.* 117 (1995) 1–19, <https://doi.org/10.1006/jcph.1995.1039>.
- [14] G. Guisbiers, L. Buchaillot, Modeling the melting enthalpy of nanomaterials, *J. Phys. Chem. C* 113 (2009) 3566–3568, <https://doi.org/10.1021/jp809338t>.
- [15] W.H. Qi, M.P. Wang, M. Zhou, X.Q. Shen, X.F. Zhang, Modeling cohesive energy and melting temperature of nanocrystals, *J. Phys. Chem. Solids* 67 (2006) 851–855, <https://doi.org/10.1016/j.jpcs.2005.12.003>.

- [16] R. Lizárraga, E. Holmström, S.C. Parker, C. Arrouvel, Structural characterization of amorphous alumina and its polymorphs from first-principles XPS and NMR calculations, *Phys. Rev. B* 83 (2011) 94201, <https://doi.org/10.1103/PhysRevB.83.094201>.
- [17] P.R. Couchman, W.A. Jesser, Thermodynamic theory of size dependence of melting temperature in metals, *Nature* 269 (1977) 481–483, <https://doi.org/10.1038/269481a0>.
- [18] C.L. Yaws, *Chemical Properties Handbook: Physical, Thermodynamic, Environmental, Transport, Safety, and Health Related Properties for Organic and Inorganic Chemicals*, McGraw-Hill, 1999.
- [19] F. Delogu, Mechanistic aspects of homogeneous and heterogeneous melting processes, *J. Phys. Chem. B* 110 (2006) 12645–12652, <https://doi.org/10.1021/jp061225k>.
- [20] A.B. Belonoshko, Molecular dynamics of MgSiO₃ perovskite at high pressures: Equation of state, structure, and melting transition, *Geochim. Cosmochim. Acta* 58 (1994) 4039–4047, [https://doi.org/10.1016/0016-7037\(94\)90265-8](https://doi.org/10.1016/0016-7037(94)90265-8).
- [21] V.S. Dozhdikov, A.Y. Basharin, P.R. Levashev, Two-phase simulation of the crystalline silicon melting line at pressures from – 1 to 3 GPa Two-phase simulation of the crystalline silicon melting line at pressures from – 1 to 3 GPa, 54502 (2014). doi:10.1063/1.4739085.
- [22] A.B. Belonoshko, Melting of corundum using conventional and two-phase molecular dynamic simulation method, *Phys. Chem. Miner.* 25 (1998) 138–141.
- [23] H. Akbarzadeh, H. Abroshan, G.A. Parsafar, Surface free energy of platinum nanoparticles at zero pressure: A molecular dynamic study, *Solid State Commun.* 150 (2010) 254–257, <https://doi.org/10.1016/j.ssc.2009.11.013>.
- [24] R. Freitas, M. Asta, M. De Koning, Nonequilibrium free-energy calculation of solids using LAMMPS, *Comput. Mater. Sci.* 112 (2016) 333–341, <https://doi.org/10.1016/j.commatsci.2015.10.050>.
- [25] W. Luo, W. Hu, S. Xiao, Size effect on the thermodynamic properties of silver nanoparticles, *J. Phys. Chem. C* 112 (2008) 2359–2369, <https://doi.org/10.1021/jp0770155>.
- [26] I.A. Aksay, J.A. Pask, R.F. Davis, Densities of SiO₂-Al₂O₃ melts, *J. Am. Ceram. Soc.* 62 (1979) 332–336.
- [27] K. Turnay, Thermophysikalische Eigenschaften des Aluminiumoxides und Quarzglases, *Res. Cent. Karlsruhe* (Mai 1985), 1985.
- [28] V.I. Levitas, M.L. Pantoya, G. Chauhan, I. Rivero, Effect of the alumina shell on the melting temperature depression for aluminum nanoparticles, *J. Phys. Chem. C* 113 (2009) 14088–14096, <https://doi.org/10.1021/jp902317m>.
- [29] P.-F. Paradis, T. Ishikawa, Y. Saita, S. Yoda, Non-contact thermophysical property measurements of liquid and undercooled alumina, *Jpn. J. Appl. Phys.* 43 (2004) 1496–1500, <https://doi.org/10.1143/JJAP.43.1496>.
- [30] W.D. Kingery, Surface tension of some liquid oxides and their temperature coefficients, *J. Am. Ceram. Soc.* 42 (1959) 6–10, <https://doi.org/10.1111/j.1151-2916.1959.tb09134.x>.
- [31] R. Bartlett, J. Hall, Wetting of several solids by Al₂O₃ and BeO liquids, *American* 44 (1965) 444.
- [32] J.J. Rasmussen, R.P. Nelson, Surface tension and density of molten Al₂O₃, *J. Am. Ceram. Soc.* 54 (1971) 398–401, <https://doi.org/10.1111/j.1151-2916.1971.tb12330.x>.
- [33] H. Von Wartenberg, G. Wehner, E. Saran, Surface tension of molten aluminum and lanthanum oxides, *Nachr. Ges. Wiss. Göttingen, Math.-Physik.* 2 (1936) 65–71.
- [34] P. Nikolopoulos, Surface, grain-boundary and interfacial energies in Al₂O₃ and Al₂O₃-Sn, Al₂O₃-Co systems, *J. Mater. Sci.* 20 (1985) 3993–4000, <https://doi.org/10.1007/BF00552390>.
- [35] R. Freitas, T. Frolov, M. Asta, Step free energies at faceted solid surfaces: Theory and atomistic calculations for steps on the Cu(111) surface, *Phys. Rev. B* 95 (2017) 155444, <https://doi.org/10.1103/PhysRevB.95.155444>.